

Microstructural Characterization and Hydrogen Storage Properties at Room Temperature of $Ti_{21}Zr_{21}Fe_{41}Ni_{17}$ Medium Entropy Alloy

Gaspar Andrade, Payam Edalati, Shivam Dangwal, Kaveh Edalati, and Ricardo Floriano*



Cite This: *ACS Appl. Energy Mater.* 2025, 8, 2033–2042



Read Online

ACCESS |

Metrics & More

Article Recommendations

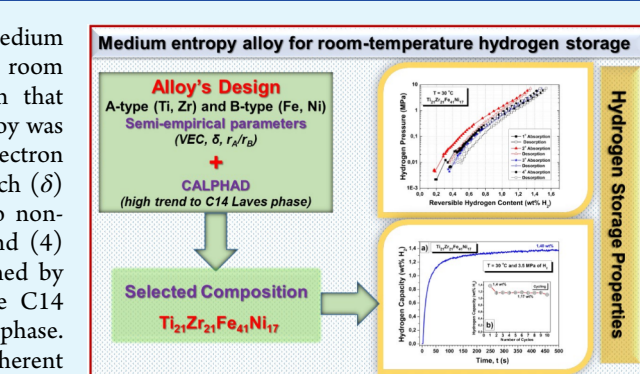
ABSTRACT: This study presents the design and evaluation of a medium entropy alloy (MEA), $Ti_{21}Zr_{21}Fe_{41}Ni_{17}$, for hydrogen storage at room temperature (30 °C), employing an integrated design approach that combines CALPHAD calculations with semiempirical rules. The alloy was developed based on four specific design criteria: (1) valence electron concentration (VEC) between 6.2 and 6.5, (2) atomic size mismatch (δ) of at least 9.7%, (3) an atomic radius ratio of hydride-forming to non-hydride-forming elements (r_A/r_B) ranging from 1.149 to 1.219, and (4) stability of the C14 Laves phase as the primary phase, as confirmed by CALPHAD. The resulting alloy crystallized predominantly in the C14 Laves phase (92.8 wt %), with a minor body-centered cubic (BCC) phase. Transmission electron microscopy (TEM) results revealed coherent nanograin boundaries, particularly at the C14/BCC interphase, facilitating rapid hydrogenation kinetics. After a one-step simple thermal activation, the alloy reversibly absorbed 1.4 wt % of hydrogen with relatively low hysteresis and fast kinetics, attributed to a preferential hydride nucleation at grain boundaries. In terms of thermodynamic properties, the chemical composition, designed according to the aforementioned criteria, should be considered, with the high iron content (41%) playing a critical role. The high atomic percentage of iron, a non-hydride-forming element, stabilizes the C14 phase due to the significant negative contribution of the interaction parameter (Ω_{ij}) of the Fe–Zr pair ($\Omega_{ij} = -118.4 \text{ kJ/mol}$), which results in a negative enthalpy of mixing in the C14 structure. This work underscores the utility of combining CALPHAD and semiempirical design methods while outlining critical challenges and future directions for optimizing MEAs for hydrogen storage.

KEYWORDS: Medium-entropy hydrides, Solid-state hydrogen storage, CALPHAD, $TiZrFeNi$, C14-Laves phase, Interphase boundaries

INTRODUCTION

High-entropy alloys (HEAs) are a new class of materials characterized by their remarkable structural and functional properties.^{1–4} Several efforts have been made to define HEAs, and it is generally accepted that they consist of at least five principal elements mixed to form a single-phase solid solution.^{5,6} The mixing entropy (ΔS_{mix}) is the thermodynamic parameter typically used to classify multiprincipal element alloys. In this context, HEAs usually fall within the range where $\Delta S_{\text{mix}} > 1.5R$ (where R is the universal gas constant). Medium-entropy alloys (MEAs) are classified when the mixing entropy lies between R and $1.5R$ ($R < \Delta S_{\text{mix}} < 1.5R$). Low-entropy alloys (LEAs) are considered those with $\Delta S_{\text{mix}} \leq R$.⁷ HEAs and MEAs are sometimes broadly categorized as multi-component alloys.⁸

Since the early 2010s, HEAs have been explored as potential materials for solid-state hydrogen storage.^{9–12} Most HEAs studied for hydrogen storage to date are solid solution alloys that incorporate elements with a strong affinity for hydrogen, such as Ti, Zr, Nb, Hf, Ta, and V.^{13–15} These elements form highly stable hydrides that require high temperatures, typically



above 400 °C, to release hydrogen, which limits the practical applications of these HEAs and their hydrides.^{16–19}

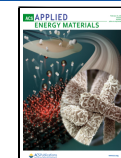
Laves phase alloys, particularly those based on the AB₂-type structure, have been extensively studied for hydrogen storage due to their high volumetric and gravimetric capacities, structural stability, and reversible hydrogen absorption/desorption behavior.^{20–22} These intermetallic compounds, such as ZrFe₂, ZrMn₂, and TiCr₂, commonly exhibit a hexagonal C14 or cubic C15 structure, which is critical for their hydrogen storage performance.^{23,24} Systematic investigations into AB₂-type high-entropy systems have revealed that their hydrogen storage properties can be significantly enhanced by optimizing key parameters such as valence electron concentration (VEC), atomic size mismatch (δ), and

Received: October 3, 2024

Revised: February 1, 2025

Accepted: February 2, 2025

Published: February 10, 2025



the ratio of hydride-forming to nonhydride-forming elements.^{25,26} For instance, as will be discussed in detail, studies on Zr-based Laves phase alloys have shown that VEC and phase stability are crucial for tailoring hydrogen sorption properties.^{27,28} While traditional AB₂ alloys like ZrCr₂ and ZrMn₂ operate effectively at elevated temperatures, recent studies employing computational approaches such as CALPHAD and first-principles calculations have facilitated the design of novel AB₂-type alloys for room-temperature hydrogen storage.^{29,18} Research on the hydrogenation behavior of Ti-based C14 Laves phase alloys demonstrated enhanced performance through alloying with Fe and Ni, improving hydrogen kinetics and reversibility.³⁰ Similarly, ZrCr₂-based alloys modified with Mn and V exhibited high hydrogen storage capacities with stable cycling performance.^{31,32} Minor substitutions with transition metals, such as Nb and Co, in AB₂-type alloys, have further shown promise for improving hydrogenation kinetics and reducing hysteresis.³³ Despite previous studies on traditional and high-entropy AB₂-type Laves phase alloys, the present study advances this field by focusing on medium-entropy alloys (MEAs), which uniquely balance entropy and enthalpy contributions, to design an AB₂-type Ti₂₁Zr₂₁Fe₄₁Ni₁₇ alloy with a dominant C14 Laves phase. By integrating semiempirical descriptors and CALPHAD modeling, a material is demonstrated capable of reversible hydrogen storage with fast kinetics and significant capacity at room temperature. This work not only underscores the utility of combining computational and experimental approaches for hydrogen storage alloy design but also highlights the novel application of MEAs within the AB₂ framework to achieve room-temperature hydrogen storage.

A key challenge in the field of hydrogen storage is discovering a material or hydride that can simultaneously meet several essential criteria. These criteria include the ability to efficiently absorb and release hydrogen at room temperature in a reversible manner, fast kinetics, easy activation, long-term cycling stability, storage at pressures near atmospheric levels, and high gravimetric capacity.^{30,34–41} Given the significant influence of alloy composition on these hydrogen storage properties, HEAs offer a vast compositional space for exploration, providing numerous opportunities to fine-tune and adjust these properties to meet the required performance standards.^{42–44}

The extensive compositional characteristics of HEAs have been partially explored using various thermodynamic-based methods, including semiempirical rules and descriptors, *ab initio* calculations, and the CALPHAD (Calculation of Phase Diagrams) approach.^{45,46} These methods hold significant potential for providing a deeper fundamental understanding of the phases present within HEA systems, their stability, and their relationship to specific desirable attributes for hydrogen storage.^{46–48} For instance, the valence electron concentration (VEC) has been linked to hydrogen storage properties, with a VEC of 6.4 suggested to favor low-temperature hydrogen absorption, good storage capacities, and near-complete reversibility.⁴⁹ Such insights can guide the design of HEAs with optimized hydrogen storage performance by focusing on key compositional parameters that enhance these characteristics.

The stability of the constituent phases within HEAs is crucial due to its significant impact on hydrogen storage properties.^{50–53} It has been demonstrated that single-phase HEAs can be formed under specific combinations of mixing

enthalpies (ΔH_{mix}), atomic size mismatches (δ), electronegativity mismatches ($\Delta \chi$), and VEC.⁵⁴ These parameters vary between solid solution alloys and intermetallic compounds, where a solid solution usually forms for $\delta \leq 6.6\%$.⁴⁹ Another important factor is the ratio of atomic radii between A and B components, where A represents elements with high hydrogen affinity, and B represents those with low hydrogen affinity. It has been established that when the atomic radius ratio of hydride-forming to nonhydride-forming element $r_A/r_B > 1.116$, multicomponent alloys form multiphase or amorphous structures rather than single-phase crystalline structures.⁵⁵ This understanding is essential for designing HEAs with optimized hydrogen storage capabilities, balancing phase stability and hydrogen absorption efficiency.

In a recent study, Ponsoni et al.⁵⁶ explored the influence of VEC, r_A/r_B , and δ , assisted by the CALPHAD method, on the phase stability of AB₂-type alloys (where A = Ti, Zr, Nb and B = V, Cr, Mn, Fe, Co, Ni, Cu, and Zn) in relation to their potential applications as hydrogen storage materials. A total of 1208 compositions (854 equiatomic and 354 nonequiatomic) were evaluated for phase stability. All 354 nonequiatomic alloys and 86 equiatomic compositions were predicted to form the C14 Laves phase. A high incidence of the C14 phase was observed for $5.8 \leq \text{VEC} \leq 7.0$ and $1.123 \leq r_A/r_B \leq 1.223$, with δ values consistently above 5.0% for Laves phase formation. Later studies have expanded this exploration to include not only AB₂-type alloys but also other stoichiometries derived from these elements.⁵⁷ However, despite these studies, the hydrogen storage properties of these alloys and the factors affecting their design remain unresolved.

In an effort to select an intermetallic C14 Laves phase based on HEAs that operate at room temperature, the authors proposed three criteria: (i) an AB₂-type configuration, (ii) a C14 Laves single-phase structure, and (iii) a VEC of 6.4. Using this approach, an AB₂-type HEA, TiZrCrMnFeNi, was designed and demonstrated 1.7 wt % of reversible hydrogen absorption at room temperature.⁵⁸ Subsequent first-principles calculations revealed that the effectiveness of these criteria was due to the low hydrogen binding energy required for room-temperature hydrogen storage,⁵⁷ a finding that was experimentally confirmed in a study on Zr-based HEAs.⁵⁹ These criteria were further generalized to other stoichiometries to select C14-based HEAs, such as TiZrNbFeCrNi,⁶⁰ TiZrNbCrFe,⁶¹ and TiZrNbFeNi.⁶² These alloys predominantly exhibited a C14 Laves phase, with a minor BCC phase. It was confirmed that when the VEC is set to values near 6.4, the alloys can reversibly absorb hydrogen with a simple activation process, mostly at room temperature and with fast kinetics.^{57–62}

While many studies have focused on the entropy of mixing due to a large number of principal elements, the enthalpy of mixing is another critical parameter in MEAs that has not been adequately considered. A deeper investigation into the role of ΔH_{mix} in stabilizing Laves-phase-based MEAs is essential for optimizing their properties for hydrogen storage. Moreover, despite recent advancements, the significance of secondary phases in C14-based alloys and their influence on hydride nucleation remain unresolved.⁵ Understanding how these secondary phases interact with the hydrogen absorption process could significantly improve the design and performance of multicomponent alloys for hydrogen storage applications. Addressing these gaps in knowledge could provide valuable insights into the thermodynamic and kinetic

behaviors of these materials, enhancing their efficiency and reversibility in hydrogen storage systems.

In this study, we propose a design strategy for MEAs for hydrogen storage, focusing on compositional and microstructural factors within a model Ti–Zr–Fe–Ni system. The alloy – $Ti_{21}Zr_{21}Fe_{41}Ni_{17}$ – was selected through the combination of semiempirical descriptors and computational thermodynamic calculations using CALPHAD, aiming to achieve the C14 Laves phase as the major phase. The alloy was synthesized by arc melting under an argon atmosphere and thoroughly characterized by using X-ray diffraction (XRD), scanning electron microscopy (SEM), and transmission electron microscopy (TEM). The hydrogen storage properties at room temperature ($30\text{ }^{\circ}\text{C}$), were systematically investigated, and the correlations between secondary phases and hydrogen storage performance were discussed.

MATERIAL AND METHODS

To select a MEA for room-temperature hydrogen storage, a semiempirical and thermodynamics-based method was applied. First, hydride-forming elements A (Ti, Zr) and nonhydride-forming elements B (Fe, Ni) were selected to combine in some different stoichiometries. In the second step, some restrictions were applied to obtain compositions with a high tendency to form the C14 Laves phase in the following order: VEC = 6.2–6.5, $\delta \geq 9.7\%$, and $r_A/r_B = 1.149–1.219$. The VEC was calculated with the weighted average of the VEC of each element in the alloy, considering their stoichiometry. For the atomic size mismatch (δ), the standard deviation of the atomic radius of the elements of the alloy. Finally, the r_A/r_B was calculated as the ratio between the average atomic radius of the elements positioned in the A sites and B sites of the C14 unit cell.

These alloys were carefully evaluated by the CALPHAD method using Thermocalc (TCHEA3 database) to check the stability of phases during the thermodynamic equilibrium and to confirm the high trend in the formation of the C14 Laves phase. Following these procedures, the $Ti_{21}Zr_{21}Fe_{41}Ni_{17}$ MEA was chosen as the object of this study, to determine its hydrogen storage properties.

The alloy was experimentally prepared through arc melting of high-purity elemental powders of Zr (99.5%), Ti (99.99%), Fe (99.97%), and Ni (99.99%). The process of arc melting was executed utilizing a nonconsumable tungsten electrode and a water-cooled copper crucible under a high-purity argon atmosphere. To enhance chemical uniformity, the ingots underwent six rotations and remelting cycles, while the mass loss was negligible. Subsequently, the ingots were cut into smaller pellets for further microstructural characterization and hydrogen storage measurements.

For crystal structure analysis, the alloy was crushed into microsized powders and subjected to XRD measurements. The XRD analysis utilized a Cu–K α radiation source ($\lambda = 0.15406\text{ nm}$) with an X’Pert Panalytical diffractometer operating at 45 kV and 40 mA. The Rietveld refinement method, in conjunction with GSAS-II software, was employed to determine the lattice parameters, phase fractions (wt %), crystallite size, and isotropic microstrain. The refinement process included adjusting the background estimation using a Chebyshev background function with five coefficients, determining phase fractions, and refining lattice parameters. The resulting refinements demonstrated residual values (R_{wp}) and goodness-of-fit (GOF) below 5%, affirming the high quality and reliability of the results.⁶³

Microstructural investigations were conducted using SEM and high-resolution TEM. For SEM, the samples underwent mechanical polishing with colloidal silica of 60 nm particle size. The polished samples were examined using a Philips XL-30 FEG SEM instrument equipped with energy-dispersive X-ray spectroscopy (EDS). Back-scattered electron and secondary electron (BSE and SE) images, along with elemental mapping at different magnifications in selected regions, were captured for all samples. For TEM analysis, ethanol was used as a medium to crush the alloy, while preventing oxidation. After being

crushed, the sample was dispersed onto a carbon grid and immediately examined by TEM.

To assess hydrogen storage performance, pressure–composition–temperature (PCT) absorption and desorption isotherms, along with kinetic measurements under a hydrogen pressure of 3.5 MPa, were carried out at $30\text{ }^{\circ}\text{C}$ (room temperature) using a Sievert-type machine from Suzuki Shokan Co., Ltd. Samples weighing approximately 250 mg were crushed in air followed by passing the crushed powders through a sieve of $75\text{ }\mu\text{m}$ size. Additionally, hydrogen absorption and desorption cycles were conducted for 10 iterations (20 min hydrogen absorption under an initial pressure of 3.5 MPa at $30\text{ }^{\circ}\text{C}$ followed by 120 min evacuation at $30\text{ }^{\circ}\text{C}$).

The hydrogenation measurements were first conducted without any activation treatment, but since the alloys did not absorb hydrogen, an activation procedure was applied. The activation procedure applied consisted of increasing the temperature to $450\text{ }^{\circ}\text{C}$ for 3 h under a dynamic vacuum and left to cool down to room temperature by itself. The simple activation procedure applied in this study proved to be effective, enabling the alloy to absorb hydrogen reversibly. Given their success, alternative activation procedures were not explored. Notably, this method is widely used and well-documented in other studies on HEAs for hydrogen storage,^{56,59–62} underscoring its reliability and practicality. It is important to mention that the activation procedure does not lead to any structural phase transitions due to the small temperature compared to the melting point of the alloys. Also, hydrogen storage tests were performed after thermal activation. XRD examined selected samples after hydrogenation, and in this case, the samples were examined by XRD in less than 5 min after their removal from the reactor of the Sieverts machine.

RESULTS

Figure 1 shows the phase diagram of the designed alloy determined by a Thermocalc. The thermodynamic computa-

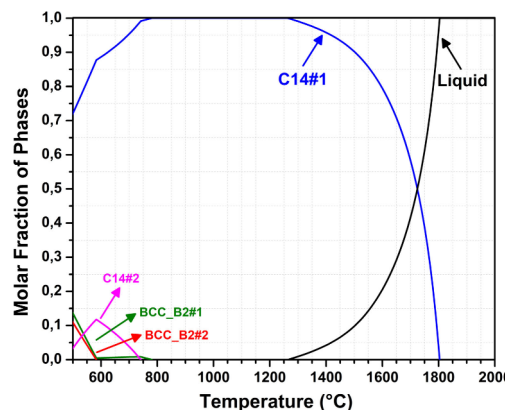


Figure 1. Molar fraction of equilibrium phases as a function of temperature calculated for the $Ti_{21}Zr_{21}Fe_{41}Ni_{17}$ alloy using the CALPHAD and TCHEA3 database.

tional calculation indicates that the alloy crystallizes with the majority of the C14 phase in the equilibrium. Furthermore, considering the large solidification interval, the C14 phase remains stable in the liquid phase and grows at elevated temperatures ($1800\text{ }^{\circ}\text{C}$) until its complete solidification. Although the thermodynamic equilibrium foresees other phases such as BCC in temperatures below $750\text{ }^{\circ}\text{C}$, their fractions are very low, under 10% of all phases.

Table 1 shows the atomic fraction of each element in the C14 phase of the referred composition determined by CALPHAD. The occupation factor of each element in the C14 unit cell was used later to determine the structural parameters by the Rietveld refinement.

Table 1. Structural Parameters of the C14 Unit Cell in the $Ti_{21}Zr_{21}Fe_{41}Ni_{17}$ Alloy

Phase	Atom	Wyckoff position	Molar fraction	Occupation factor
C14 Space Group: P6 ₃ /mmc (194)	Zr	4f (1/3, 2/3, 0.06030)	0.21	0.62
	Ti		0.21	0.38
	Fe	2a (0, 0, 0)	0.41	0.61
	Ni		0.17	0.26
	Ti		----	0.13
	Fe	6h (0.83170, 0.66340, 1/4)	----	0.61
	Ni		----	0.26
	Ti		----	0.13

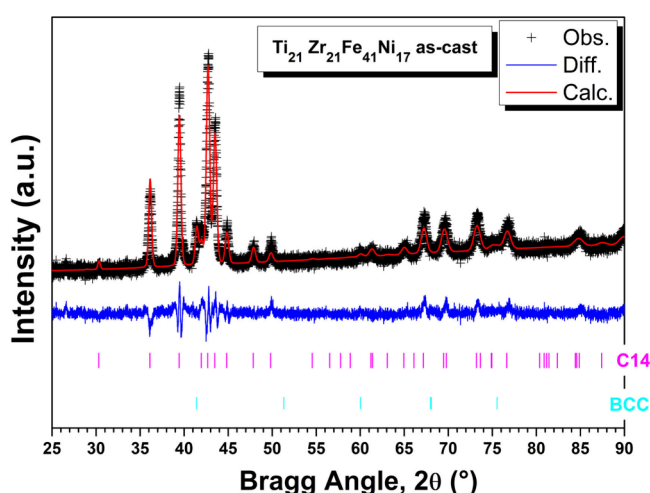
**Figure 2.** XRD pattern and Rietveld refinement of the $Ti_{21}Zr_{21}Fe_{41}Ni_{17}$ alloy in the as-cast condition.

Figure 2 and Figure 3 show the XRD patterns with the corresponding Rietveld refinement and SEM/EDS images of the $Ti_{21}Zr_{21}Fe_{41}Ni_{17}$ alloy, respectively. The Rietveld refinement was done by using the crystal structure data displayed in Table 1 which was built by using the information on the composition and the constitution of the calculated C14 Laves phase at 1000 °C. The agreement indices for the refinement are GOF = 1.45 and Rwp = 3.022. The structural parameters of the C14 phase, as determined by Rietveld, are $a = 4.968$ and $c = 8.079$ Å. The Rietveld refinement indicates that the alloy crystallizes as a major C14 phase –92.8 wt % – and a minor BCC phase –7.2 wt %, in good agreement with the calculated phase diagram in Figure 1. These results agree with the SEM images shown in Figure 3-a and Figure 3-b, where it is evident that there is the existence of a two-phase microstructure. The elemental mappings shown in Figure 3 suggest that some elements tend to occupy one phase instead of another. For example, a higher concentration of Ni and Ti in the dark regions detached in Figure 3-b is observed, while at the same time, these areas are poor in Fe. On the other hand, Zr is very well distributed in the whole microstructure, meaning that this element is present in both C14 and BCC phases. It should also be noted in the EDS spectra taken from the whole area in Figure 3-c that the atomic fraction of each element is very close to the nominal percentage of these elements in the preferred alloy.

Figure 4 shows TEM images: a) bright field (BF), b) SAED pattern, and c) dark field (DF) of the $Ti_{21}Zr_{21}Fe_{41}Ni_{17}$ alloy in the as-cast state. The DF image was taken from the location of the diffracted rays indicated by the yellow arrow in the SAED pattern. The high-resolution TEM image in Figure 4-d shows some nanograins, where the crystal directions are indexed using the fast Fourier transform (FFT) analysis. As can be seen, both BCC and C14 Laves phases are crystallized next to each other in this type of grain. Figure 4-e and Figure 4-f show the two grain boundaries selected with yellow squares at a higher magnification. Figure 4-g shows one of these larger grains that contains a dislocation. Figure 4-h, prepared by using the Inverse FFT technique from the yellow square area, clearly shows the existence of this dislocation.

Regarding the hydrogen absorption properties, PCT isotherm measurements were conducted for the $Ti_{21}Zr_{21}Fe_{41}Ni_{17}$ alloy in the as-cast state at room temperature of 30 °C without any activation procedure. The sample did not show any absorption ability in this condition, and thus, the activation procedure at 450 °C for 3 h under dynamic vacuum was applied. Figure 5 shows the fourth PCT absorption and desorption isotherms of the $Ti_{21}Zr_{21}Fe_{41}Ni_{17}$ alloy at room temperature after the activation procedure. First, by looking at all PCT absorption and desorption isotherms, the absence of a well-defined equilibrium plateau pressure is evident. Second, the alloy starts to absorb hydrogen at very low pressure, on the order of kilopascal, in the first absorption, which is below the detection limit of the instrument. This fact explains why the PCT measurements did not start from zero hydrogen content. The alloy absorbs 1.4 wt % of hydrogen (subtracted from the initial 0.2 wt %) and showed a very good reversibility at room temperature, desorbing almost the same amount of hydrogen in all cycles.

Additionally, it is noteworthy that there's a slight shift in the position of the curves along the 'x' axis observed in the PCT curves. This shift is attributed to the decline in hydrogen capacity throughout the PCI cycles, a trend also observed during the kinetic cycling discussed ahead.

Figure 6-a shows the absorption kinetics of the $Ti_{21}Zr_{21}Fe_{41}Ni_{17}$ alloy at room temperature of 30 °C under a hydrogen pressure of 3.5 MPa after PCT isotherm measurements. As can be shown, the alloy exhibits a very fast absorption kinetics without any incubation time, reaching a maximum hydrogen capacity of 1.4 wt % within approximately 500 s. The cycling test applied to this alloy, as highlighted in Figure 6-b, reveals that the hydrogen storage capacity is reasonably stable after ten cycles. The maximum capacity of 1.17 wt % of H₂ remains stable between the second and the 10th cycles, while a small drop in the capacity can be noticed between the first and the second cycles.

The crystal structure of the alloy after hydrogenation was also checked. For comparison, Figure 7 shows the XRD patterns and indexed phases of the alloy in the as-cast state and after hydrogenation. As seen in the image, there is no shift in the angular positions of the C14 peaks after hydrogenation compared to the as-cast sample, which means that the alloy immediately releases hydrogen when exposed to atmospheric pressure, even considering the short time between its removal from the reactor and the XRD analysis. The cell parameters for C14 after "spontaneous" desorption are $a = 4.979$ Å and $c = 8.096$ Å, which are very close to the cell parameters obtained for the as-cast sample. In addition to the detection of the C14 phase, the presence of the BCC phase is also noticed, in

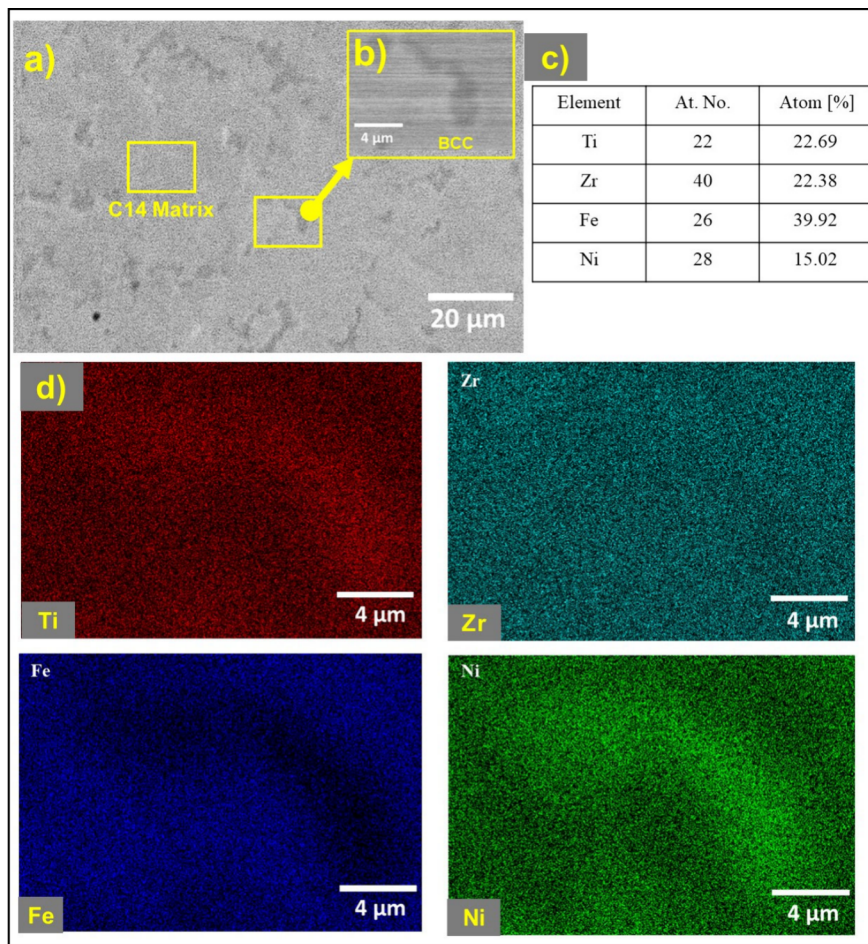


Figure 3. SEM images and corresponding EDS elemental mappings of the $\text{Ti}_{21}\text{Zr}_{21}\text{Fe}_{41}\text{Ni}_{17}$ alloy in the as-cast condition. a) SEM images using BSE mode, b) magnified view of BSE image, c) EDS quantification and d) elemental maps of the selected BSE area in (b).

agreement with Figure 2. Regarding the BCC phase, there is a small peak around 40.3° (highlighted with the symbol, o) in the hydrogenated sample that could be associated with a possible trap of hydrogen atoms in the BCC-phase forming a distorted BCC structure. This result supports the notion that hydrogen absorption induces distortions in the lattice, affecting the peak position. However, no evidence was found to indicate a phase transformation from BCC to FCC. Instead, the data only confirms a peak shift within the BCC phase, attributed to lattice distortion due to hydrogen incorporation aligned with the previous studies.^{58–62}

DISCUSSION

Intermetallic HEAs having the C14 Laves structure as the major phase demonstrated a great ability to absorb and desorb hydrogen at low temperatures,⁶⁴ with easy activation.⁵⁸ However, studies on MEAs, in which the entropy is lower and the enthalpy is more dominant, for hydrogen storage at room temperature are limited. In this study, we applied the combination of semiempirical descriptors followed by the CALPHAD thermodynamic calculations to design a MEA for hydrogen storage. The results concerning the crystal structure initially predicted using the CALPHAD method (Figure 1) and subsequently by the XRD (Figure 2), confirmed that the design method applied to the Ti–Zr–Fe–Ni system could provide a $\text{Ti}_{21}\text{Zr}_{21}\text{Fe}_{41}\text{Ni}_{17}$ alloy with a high tendency to form the majority of the C14 Laves phase stable in the

thermodynamic equilibrium. In this section, some structural and microstructural features of the designated alloy and their influence on hydrogen storage properties need to be discussed.

The microstructural analysis represented by the SEM images (Figure 3) showed the appearance of two distinct regions: dark and gray regions. The dark regions refer to the Ti-and Ni-rich regions, which are expected for the composition of the BCC phase according to the CALPHAD prediction. Moreover, the apparent amount of the BCC phase is compatible with the quantity of this phase, as determined by the Rietveld refinement. On the other hand, the gray regions that appear in high proportion in the SEM images are associated with the C14 phase. The absence of Fe in the BCC phase and its abundant presence in the C14 Laves phases are noted in EDS analysis. As we will explain later, Fe is responsible for decreasing the enthalpy of the mixture, favoring the crystallization of intermetallic phases, such as the C14 phase.

From the TEM analysis (Figure 4), it can be seen that the grains have crystallized in various sizes ranging from micrometers to nanometers, which is slightly abnormal for the sample after casting. One explanation remains for the possible small solidification interval of the alloy, as seen in Figure 1. The C14 phase nucleates with a small amount of free energy right before the end of the liquidus line. In this case, the undercooling provided by the water-cooled crucible during arc melting causes a high rate of nucleation specially for small samples, preventing the grains from growing, at least the grains

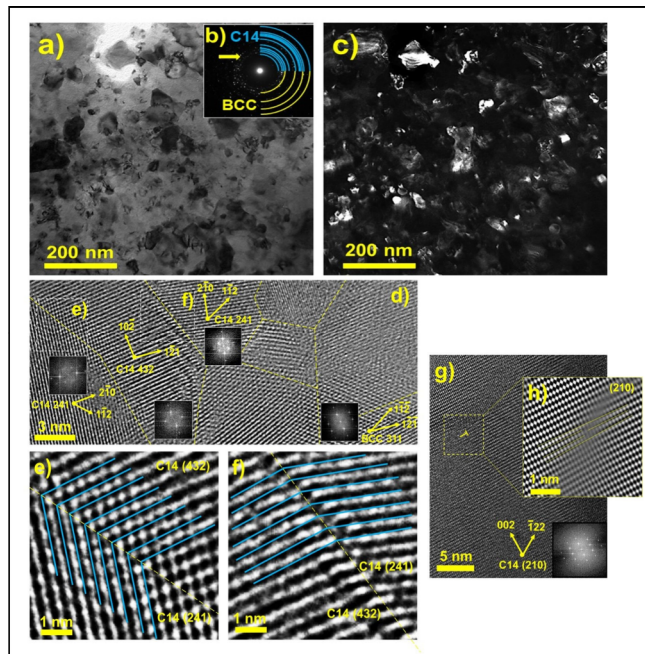


Figure 4. TEM images of the $\text{Ti}_{21}\text{Zr}_{21}\text{Fe}_{41}\text{Ni}_{17}$ alloy in the as-cast state. a) BF image, b) SAED pattern, c) DF image, d) high-resolution image showing nanoscale C14 and BCC grains, e-f) lattice images showing coherent grain boundaries, and g-h) high-resolution image and corresponding inverse FFT analysis showing dislocations in large grains.

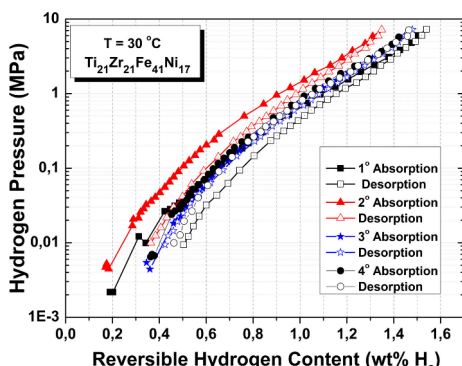


Figure 5. PCT absorption/desorption isotherms at room temperature ($30\text{ }^{\circ}\text{C}$) for the $\text{Ti}_{21}\text{Zr}_{21}\text{Fe}_{41}\text{Ni}_{17}$ alloy after activation.

under the surface.⁶⁵ The SAED analysis with a ring pattern (Figure 4-b) clearly shows the existence of nanograins of two phases, BCC and C14-Laves, which is consistent with the prediction of thermodynamic simulation with the CALPHAD method and the results of XRD analysis. It is important to pay attention to the grain boundaries of these nanograins, because they show a strong tendency to form coherent grain boundaries with low energy. Unlike large grains, dislocations are not seen in nanograins, which is expected due to the instability of dislocations near grain boundaries.

The PCT cycles of absorption and desorption (Figure 5) show that the alloy can reversibly absorb and desorb a reasonable amount of hydrogen with almost no hysteresis. It is worth pointing out that the alloy became fully activated after a one-step simple thermal activation procedure as already described in the experimental section. The absence of a well-defined plateau in the PCT curves suggests that hydrogen

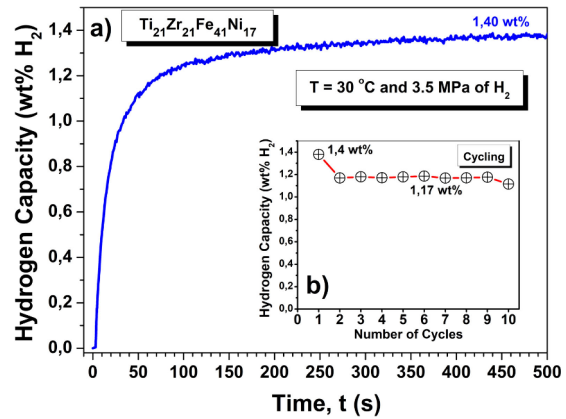


Figure 6. a) Kinetic curve of $\text{Ti}_{21}\text{Zr}_{21}\text{Fe}_{41}\text{Ni}_{17}$ alloy at room temperature ($30\text{ }^{\circ}\text{C}$) under the hydrogen pressure of 3.5 MPa , b) the hydrogen storage capacity as a function of the number of cycles.

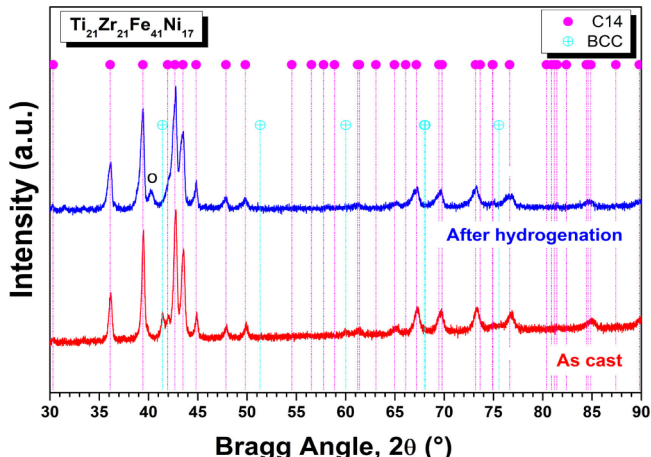


Figure 7. XRD patterns of the $\text{Ti}_{21}\text{Zr}_{21}\text{Fe}_{41}\text{Ni}_{17}$ alloy in the as-cast and hydrogenated states. Bragg angle positions for C14 and BCC phases were also included as references.

atoms form a solid solution with metallic atoms. This implies that the C14 phase absorbs hydrogen only through the dissolution of hydrogen in the C14 phase, leading to a gradual expansion of the C14 lattice parameters without any plateau pressure between the metal and hydride states. Similar PCT behavior, characterized by the presence of a sloping plateau, has been reported for many other C14-type Laves phase HEA-based alloys.^{9,11,15,56,60–62,64} However, experimental PCT curves from some C14 HEAs show a flat plateau pressure, as seen in alloys like TiZrCrMnFeNi ⁵⁸ and ZrCrMnFeNi .⁵⁹ However, even in these alloys, the hydride state is an expanded C14 phase, as confirmed by XRD after hydrogenation. This flat plateau suggests a less gradual phase separation between metallic and hydride C14 phases, which may indicate the existence of a hydrogen miscibility gap within the C14 Laves phase.⁵⁶ As mentioned earlier, the absence of an expanded C14 phase in the XRD profiles taken after hydrogenation is due to the fast hydrogenation and dehydrogenation rate of this material. Taking the pressure of 0.1 MPa (1 atm) as a reference line in Figure 5, most parts of the PCT curves are above this level of hydrogen pressure. Under an air atmosphere with a partial hydrogen pressure of almost zero, it is natural that the hydrogenated alloy tends to desorb hydrogen very fast. This fast dehydrogenation is desirable for hydrogen storage

applications, although it makes experimental problems in retaining the hydride phase for XRD analysis.

In terms of kinetics (Figure 6), the selected alloy showed a very fast hydrogen absorption after the thermal activation step. The maximum amount absorbed of 1.4 wt % of hydrogen is comparable with other C14-based alloys already reported in the literature. The TiZrNbCrFe⁶¹ alloy was able to absorb 1.35 wt % of H₂ at room temperature, while the TiZrNbFeNi⁶² absorbed 1.2 wt % of H₂ at room temperature, after the same heat treatment activation of 450 °C for 3 h in a vacuum. Also, the maximum amount of hydrogen remains almost the same after the second cycle. This feature can be attributed to the stability of the C14 phase under hydrogenation/dehydrogenation, since the reaction occurs in a single step, without any intermediate hydride phase.⁶⁶

It is important to note that the maximum theoretical hydrogen capacity of the alloy, assuming an H/M ratio of 1, is approximately 1.61 wt % of H₂, which is about 15% higher than the maximum hydrogen capacity of 1.4 wt % of H₂ measured in the alloy. Despite the alloy's immediate absorption after a simple activation process, we believe that not all interstitial sites were accessible to hydrogen, likely due to local variations in chemical composition. However, according to the PCT graph in Figure 5, the alloy has the potential to absorb nearly 1.6 wt % of H₂ at higher pressures. Further optimization of the chemical composition using lighter metals could improve the hydrogen absorption capacity of the alloy.

Assuming that the C14 Laves phase is directly responsible for the reversible hydrogen capacity, the observed decrease in capacity from 1.4 to 1.2 wt % of H₂ during cycling (Figure 6b) could be attributed to hydrogen atoms becoming trapped in the BCC phase, as indicated by the XRD pattern of the sample in the hydrogenated state (Figure 7). This behavior has also been observed in previous studies.^{59–62}

From a thermodynamic point of view, the reversibility of the alloy can be associated with the calculated value of VEC = 6.5. It was proposed that VEC should be kept around 6.4 to improve the hydrogen storage properties.^{58,61,62} Also, the calculated enthalpy of the mixture (ΔH_{mix}) for the Ti₂₁Zr₂₁Fe₄₁Ni₁₇ alloy is equal to -29 kJ/mol. The Laves phases-based HEAs with ΔH_{mix} of -15 to -5 kJ/mol are usually considered suitable candidates for hydrogen storage applications as they demonstrate high hydrogen-to-metal (H/M) ratios and favorability for hydride formation enthalpy (ΔH_{form}).^{67,68} A very negative enthalpy of formation, such as -29 kJ/mol, means that the metallic bonds are strong. According to Miedema's scheme, there is an inverse relationship between the stability of an intermetallic compound and the stability of the hydride it forms. A stable intermetallic compound tends to produce a weakly and unstable hydride. For the investigated alloy, we calculated a mixing enthalpy of -29 kJ/mol, which is significantly negative. This indicates a highly stable intermetallic compound. Following Miedema's rule, the corresponding hydride is expected to exhibit weak bonding and reduced stability.⁶⁹ It should be noted that the strong negative ΔH_{mix} calculated for this alloy with high Fe content (41 at%) comes from the elevated contribution of the interaction parameter (Ω_{ij}) of the pair Fe–Zr, where $\Omega_{ij} = -118.4 \text{ kJ/mol}$. The interaction parameters of Zr–Ni (-236.4 kJ/mol) and Ti–Ni (-124.1 kJ/mol) are also significant, but the small atomic percentage of Ni in the alloy tends to decrease its contribution to the final value of the mixing enthalpy. The

other contributions are too small, as follows for Zr–Ti (-0.8 kJ/mol), Fe–Ti (-61.6 kJ/mol), and Fe–Ni (-6.4 kJ/mol). The interaction parameters were calculated using an empirical approach based on the method outlined in the study performed by Takeuchi and Inoue.⁷⁰

Moreover, the Ti₂₁Zr₂₁Fe₄₁Ni₁₇ alloy can be classified as a MEA ($\Delta S_{\text{mix}} = 8.3 \text{ J/mol}\cdot\text{K}$ which is lower than $1.5R$, where $R = 8.31 \text{ J/mol}\cdot\text{K}$), the strongly negative ΔH_{mix} plays the main role in stabilizing the intermetallic C14 phase. Taking all together, the high concentration of Fe—a non-hydride-forming element—is responsible not only for the good reversibility of the alloy, but also for the stabilization of the C14 phase, which grants good hydrogen absorption properties.

Regarding the mechanisms that could explain the attractive hydrogen storage properties of this new Ti₂₁Zr₂₁Fe₄₁Ni₁₇ alloy, three main reasons are presented here: (i) appropriate thermodynamics of the system which was adjusted by semiempirical descriptors and thermodynamic calculations, (ii) the presence of interphase boundaries; and (iii) the presence of coherent grain boundaries. In a recent study,⁷¹ it was suggested that the presence of a small amount of a second phase appears to be a good solution to the issue of the activation of some alloys.⁷² This is supported by the fact that the interphase boundaries can act like a hydrogen transport medium, which explains the easy activation of dual-phase alloys.⁷³ However, it was claimed that the presence of interphase boundaries is not the only mechanism that explains the easy activation in HEAs, because they can also amplify the heterogeneous nucleation of the hydride at grain boundaries. The TEM images showed the presence of nanograins with a strong tendency to form coherent grain boundaries between the C14 grains. A close look at Figure 4-d shows that even some C14/BCC interphase boundaries are coherent. The nucleation of the hydride can be favored due to the reduction of energy of the grain boundaries, which explains the fast kinetics and good reversibility of the alloy. Moreover, the presence of nanoscale grains in large quantities means more grain boundaries than expected for large grains, acting as a pathway for hydrogen transport from the surface to the bulk. Even though low-angle coherent grain boundaries are less favorable to nucleate the hydride phase than high-angle grain boundaries, some studies demonstrated that coherent grain boundaries are more favorable to promote the diffusion of hydrogen atoms to the bulk, because of their highly symmetrical interstitial positions.^{74,75} In the case of MEAs, a recent contribution also shows the presence of nanograins with coherent grain boundaries for ZrNbFeCo alloy.⁷⁶ The ZrNbFeCo alloy demonstrated a hydrogen absorption capacity of up to 1.2 wt % of H₂ (hydrogen-to-metal ratio H/M ~ 0.9), with rapid absorption kinetics, achieving approximately 87% of its maximum capacity within just 60 s. Additionally, the ZrNbFeCo alloy exhibited full reversibility and excellent stability over multiple absorption–desorption cycles at room temperature, maintaining an average absorption capacity of 1.1 wt % (H/M ~ 0.82) after eight cycles.⁷⁶ Despite the promising performance of the ZrNbFeCo alloy,⁷⁶ the Ti₂₁Zr₂₁Fe₄₁Ni₁₇ alloy demonstrates significantly superior results.

Taken together, this study introduces some concepts into the design of new hydrogen storage materials. A combination of concepts developed in this study with those reported in earlier publications using experiments,⁷⁷ machine learning^{78,79} and first-principles calculations⁷⁸ is expected to further

contribute to the design of new hydrogen storage materials with high potential for practical applications.

CONCLUSIONS

This study reported the microstructural characterization and the hydrogen storage properties of an original $Ti_{21}Zr_{21}Fe_{41}Ni_{17}$ MEA, designed by the combination of semiempirical descriptors (valence electron concentration, atomic size mismatch, and atomic radius ratio of hydride-forming to non-hydride-forming element), and CALPHAD method was investigated. The alloy showed fast kinetics and could reversibly absorb 1.4 wt % of hydrogen at room temperature with a relatively small hysteresis along the cycles. The structural measurements by the Rietveld refinement show the alloy crystallizes as 92.8% of the C14 phase and a minor amount of the BCC phase, in agreement with the phase diagram obtained by the thermodynamic calculations. Additionally, nanoscale grains were observed with coherent interphase grain boundaries. It was proposed that the hydride phase nucleates preferably in grain boundaries, which explains the fast kinetics of the alloy. The applied empirical descriptors and thermodynamic computational calculations to select the C14-based alloy in this study can be principally used to design other MEAs from other systems for hydrogen storage.

AUTHOR INFORMATION

Corresponding Author

Ricardo Floriano – Postgraduate Program in Mechanical Engineering, School of Mechanical Engineering, University of Campinas (FEM-UNICAMP), 13083-860 Campinas, São Paulo, Brazil; School of Applied Sciences, University of Campinas (FCA-UNICAMP), 13484-350 Limeira, Brazil; orcid.org/0000-0002-4570-105X; Email: rflorian@unicamp.br

Authors

Gaspar Andrade – Postgraduate Program in Mechanical Engineering, School of Mechanical Engineering, University of Campinas (FEM-UNICAMP), 13083-860 Campinas, São Paulo, Brazil; School of Applied Sciences, University of Campinas (FCA-UNICAMP), 13484-350 Limeira, Brazil

Payam Edalati – Postgraduate Program in Mechanical Engineering, School of Mechanical Engineering, University of Campinas (FEM-UNICAMP), 13083-860 Campinas, São Paulo, Brazil; School of Applied Sciences, University of Campinas (FCA-UNICAMP), 13484-350 Limeira, Brazil

Shivam Dangwal – WPI, International Institute for Carbon-Neutral Energy Research (WPI-I2CNER) and Department of Automotive Science, Graduate School of Integrated Frontier Sciences, Kyushu University, Fukuoka 819-0395, Japan

Kaveh Edalati – WPI, International Institute for Carbon-Neutral Energy Research (WPI-I2CNER) and Department of Automotive Science, Graduate School of Integrated Frontier Sciences, Kyushu University, Fukuoka 819-0395, Japan

Complete contact information is available at:
<https://pubs.acs.org/10.1021/acsaem.4c02468>

Funding

The Article Processing Charge for the publication of this research was funded by the Coordination for the Improvement

of Higher Education Personnel - CAPES (ROR identifier: 00x0ma614).

Notes

The authors declare no competing financial interest.

ACKNOWLEDGMENTS

This work is supported in part by a grant from the Brazilian Research Funding Agency FAPESP (No.#2022/01351-0 and No.#2023/02216-2), and in part by Grants-in-Aid for Scientific Research on Innovative Areas from the MEXT, Japan (JP19H05176 & JP21H00150).

REFERENCES

- (1) Cantor, B.; Chang, I. T. H.; Knight, P.; Vincent, A. J. Microstructural Development in Equiatomic Multicomponent Alloys. *Mater. Sci. Eng.* **2004**, *375–377*, 213–218.
- (2) Ye, Y.; Wang, Q.; Lu, L.; Liu, C.; Yang, Y. High-Entropy Alloy: Challenges and Prospects. *Mater. Today* **2016**, *19*, 349–362.
- (3) Miracle, D. B.; Senkov, O. N. A Critical Review of High-Entropy Alloys and Related Concepts. *Acta Mater.* **2017**, *122*, 448–511.
- (4) Marques, F.; Balcerzak, M.; Winkelmann, F.; Zepon, G.; Felderhoff, M. Review and Outlook on High-Entropy Alloys for Hydrogen Storage. *Energy Environ. Sci.* **2021**, *14*, 5191–5227.
- (5) Luo, L.; Chen, L.; Li, L.; Liu, S.; Li, Y.; Li, C.; Li, L.; Cui, J.; Li, Y. High-Entropy Alloys for Solid Hydrogen Storage: A Review. *Int. J. Hydrogen Energy* **2024**, *50*, 406–430.
- (6) Somo, T. R.; Lototskyy, M. V.; Yartys, V. A.; Davids, M. W.; Nyamsi, S. N. Hydrogen Storage Behaviours of High Entropy Alloys: A Review. *J. Energy Storage* **2023**, *73*, No. 108969.
- (7) Yao, K.-F.; Luan, H.-W.; Shao, Y.; Li, J.-F.; Mao, W.-L.; Han, Z. D.; Shao, C. Phase Stabilities of High Entropy Alloys. *Scr. Mater.* **2020**, *179*, 40–44.
- (8) Akrami, A.; Edalati, P.; Fuji, M.; Edalati, K. High-Entropy Ceramics: Review of Principles, Production, and Applications. *Mater. Sci. Eng.* **2021**, *146*, No. 100644.
- (9) Kunce, I.; Polanski, M.; Bystrzycki, J. Structure and Hydrogen Storage Properties of a High Entropy $ZrTiVCrFeNi$ Alloy Synthesized Using Laser Engineered Net Shaping (LENS). *Int. J. Hydrogen Energy* **2013**, *38*, 12180–12189.
- (10) Wang, Y.; Yuan, J.; Chen, J.; Li, Z.; Huang, H.; Lv, Y.; Liu, B.; Li, Y.; Wu, Y. Superior Cycle Life of $TiZrFeMnCrV$ High Entropy Alloy for Hydrogen Storage. *Scr. Mater.* **2022**, *212*, No. 114548.
- (11) Chen, S.-K.; Lee, P.-H.; Lee, H.; Su, H.-T. Hydrogen Storage of C14-Cr_xFe_yMn_zTixVyZrz Alloys. *Mater. Chem. Phys.* **2018**, *210*, 336–347.
- (12) King, D. J. M.; Middleburgh, S. C.; McGregor, A. G.; Cortie, M. B. Predicting the Formation and Stability of Single-Phase High-Entropy Alloys. *Acta Mater.* **2016**, *104*, 172–179.
- (13) Yang, X.; Zhang, Y. Prediction of High-Entropy Stabilized Solid-Solution in Multi-Component Alloys. *Mater. Chem. Phys.* **2012**, *132*, 233–238.
- (14) Guruvidyathri, K.; Vaidya, M.; Murty, B. S. Challenges in Design and Development of High-Entropy Alloys: A Thermodynamic and Kinetic Perspective. *Scr. Mater.* **2020**, *188*, 37–43.
- (15) Kao, Y. F.; Chen, S. K.; Sheu, J. H.; Lin, J. T.; Lin, W. E.; Yeh, J. W.; Lin, S. J.; Liou, T. H.; Wang, C. W. Hydrogen Storage Properties of Multi-Principal-Component CoFeMnTixVyZrz Alloys. *Int. J. Hydrogen Energy* **2010**, *35*, 9046–9059.
- (16) Nygård, M. M.; Ek, G.; Karlsson, D.; Sørby, M. H.; Sahlberg, M.; Hauback, B. C. Counting Electrons: A New Approach to Tailor the Hydrogen Sorption Properties of High-Entropy Alloys. *Acta Mater.* **2019**, *175*, 121–129.
- (17) Nygård, M. M.; Ek, G.; Karlsson, D.; Sørby, M. H.; Sahlberg, M.; Hauback, B. C. Hydrogen Storage in High-Entropy Alloys with Varying Degree of Local Lattice Strain. *Int. J. Hydrogen Energy* **2019**, *44*, 29140–29149.

- (18) Sahlberg, M.; Karlsson, D.; Zlotea, C.; Jansson, U. Superior Hydrogen Storage in High-Entropy Alloys. *Sci. Rep.* **2016**, *6*, 36770.
- (19) Zhang, C.; Song, A.; Yuan, Y.; Wu, Y.; Zhang, P.; Lu, Z.; Song, X. Study on the Hydrogen Storage Properties of a TiZrNbTa High-Entropy Alloy. *Int. J. Hydrogen Energy* **2020**, *45*, 5367–5374.
- (20) Kandavel, M.; Bhat, V. V.; Rougier, A.; Aymard, L.; Nazri, G. A.; Tarascon, J. M. Improvement of Hydrogen Storage Properties of the AB₂ Laves Phase Alloys for Automotive Application. *Int. J. Hydrogen Energy* **2008**, *33*, 3754–3761.
- (21) Ulmer, U.; Dieterich, M.; Pohl, A.; Dittmeyer, R.; Linder, M.; Fichtner, M. Study of the Structural, Thermodynamic and Cyclic Effects of Vanadium and Titanium Substitution in Laves-Phase AB₂ Hydrogen Storage Alloys. *Int. J. Hydrogen Energy* **2017**, *42*, 20103–20110.
- (22) Wang, H.; Tang, A. C.; Wan, C. B.; Yin, W. X.; Wang, Y. T.; Ju, X. Synergistic Effect for Improving the Hydrogen Storage Capability and Electrochemical Performance of AB₂ Laves Phase Alloys. *J. Alloys Compd.* **2023**, *964*, No. 171219.
- (23) Zhao, H.; Yao, P.; Zhao, Y.; Zeng, Z.; Xia, C.; Yang, T. Microstructure and Hydrogen Storage Properties of Zr-Based AB₂-Type High-Entropy Alloys. *J. Alloys Compd.* **2023**, *960*, No. 170665.
- (24) Akiba, E.; Iba, H. Hydrogen absorption by Laves phase related BCC solid solution. *Intermetallics* **1998**, *6*, 461–470.
- (25) Liang, J.; Li, G.; Ding, X.; Li, Y.; Wen, Z.; Zhang, T.; Qu, Y. Effect of C₁₄ Laves/BCC on Microstructure and Hydrogen Storage Properties of (Ti_{32.5}V_{27.5}Zr₇.5Nb_{32.5})_{1-x}Fex ($x = 0.03, 0.06, 0.09$) High-Entropy Hydrogen Storage Alloys. *J. Energy Storage* **2023**, *73*, No. 108852.
- (26) Mohammadi, A.; Ikeda, Y.; Edalati, P.; Mito, M.; Grabowski, B.; Li, H.-W.; Edalati, K. High-Entropy Hydrides for Fast and Reversible Hydrogen Storage at Room Temperature: Binding-Energy Engineering via First-Principles Calculations and Experiments. *Acta Mater.* **2022**, *236*, No. 118117.
- (27) Komeili, M.; Arabi, H.; Pourarian, F. Structural Investigation and Hydrogenation Properties of TiZrXMnFeNi (X = Cr, Mo, and W) High-Entropy Alloys. *J. Alloys Compd.* **2023**, *967*, No. 171672.
- (28) Dangwal, S.; Ikeda, Y.; Grabowski, B.; Edalati, K. Machine Learning to Design High-Entropy Alloys with Desired Enthalpy for Room-Temperature Hydrogen Storage: Comparison with Density Functional Theory and Experiments. *Chem. Eng. J.* **2024**, *493*, No. 152606.
- (29) Gesari, S. B.; Pronzato, M. E.; Visintin, A.; Juan, A. Hydrogen Storage in AB₂ Laves Phase (A = Zr, Ti; B = Ni, Mn, Cr, V): Binding Energy and Electronic Structure. *J. Phys. Chem. C* **2010**, *114* (39), 16832–16836.
- (30) Maeda, T.; Fuura, T.; Matsumoto, I.; Kawakami, Y.; Masuda, M. Cyclic Stability Test of AB₂-Type Alloys for Stationary Hydrogen Storage in Water-Contaminated Hydrogen. *J. Alloys Compd.* **2013**, *580*, S255–S258.
- (31) Møller, K. T.; Jensen, T. R.; Akiba, E.; Li, H.-W. Hydrogen - A sustainable energy carrier. *Progress in Natural Science: Materials International* **2017**, *27*, 34–40.
- (32) Yang, F.; Wang, J.; Zhang, Y.; Wu, Z.; Zhang, Z.; Zhao, F.; Huot, J.; Novaković, J. G.; Novaković, N. Recent progress on the development of high entropy alloys (HEAs) for solid hydrogen storage: A review. *Int. J. Hydrogen Energy* **2022**, *47*, 11236–11249.
- (33) Yartys, V. A.; Lototskyy, M. V. Laves type intermetallic compounds as hydrogen storage materials: A review. *J. Alloys compd.* **2022**, *916*, 165219.
- (34) Zlotea, C.; Sow, M. A.; Ek, G.; Couzinié, J. P.; Perrière, L.; Guillot, I.; Bourgon, J.; Møller, K. T.; Jensen, T. R.; Akiba, E.; Sahlberg, M. Hydrogen Sorption in TiZrNbHfTa High-Entropy Alloy. *J. Alloys Compd.* **2019**, *775*, 667–674.
- (35) Chanchetti, L.; Oviedo Diaz, S. M.; Milanez, D. H.; Leiva, D. R.; De Faria, L. I. L.; Ishikawa, T. Technological Forecasting of Hydrogen Storage Materials Using Patent Indicators. *Int. J. Hydrogen Energy* **2016**, *41*, 18301–18310.
- (36) Hirscher, M.; Yartys, V. A.; Baricco, M.; Von Colbe, J. B.; Blanchard, D.; Bowman, R. C., Jr.; Broom, D. P.; Buckley, C. E.; Chang, F.; Chen, P.; Cho, Y. W.; Crivello, J.-C.; Cuevas, F.; David, W. I. F.; De Jongh, P. E.; Denys, R. V.; Dornheim, M.; Felderhoff, M.; Filinchuk, Y.; Froudakis, G. E.; Grant, D. M.; Gray, E. M. A.; Hauback, B. C.; He, T.; Humphries, T. D.; Jensen, T. R.; Kim, S.; Kojima, Y.; Latroche, M.; Li, H.-W.; Lototskyy, M. V.; Makepeace, J. W.; Møller, K. T.; Naheed, L.; Ngene, P.; Noreus, D.; Nygård, M. M.; Orimo, S.; Paskevicius, M.; Pasquini, L.; Ravnsbæk, D. B.; Sofianos, M. V.; Udrovic, T. J.; Vegge, T.; Walker, G. S.; Webb, C. J.; Weidenthaler, C.; Zlotea, C. Materials for Hydrogen-Based Energy Storage: Past, Recent Progress, and Future Outlook. *J. Alloys Compd.* **2020**, *827*, No. 153548.
- (37) Huot, J.; Cuevas, F.; Deledda, S.; Edalati, K.; Filinchuk, Y.; Grosdidier, T.; Hauback, B.; Heere, M.; Jensen, T. R.; Latroche, M.; Sartori, S. Mechanochemistry of Metal Hydrides: Recent Advances. *Materials* **2019**, *12*, 2778.
- (38) Cohen, R.; West, K.; Wernick, J. Degradation of LaNi₅ by Temperature-Induced Cycling. *J. Less-Common Met.* **1980**, *73*, 273–279.
- (39) Zhao, X.; Zhou, J.; Shen, X.; Yang, M.; Ma, L. Structure and Electrochemical Hydrogen Storage Properties of A2B-Type Ti-Zr-Ni Alloys. *Int. J. Hydrogen Energy* **2012**, *37*, 5050–5055.
- (40) Schlapbach, L.; Riesterer, T. The Activation of FeTi for Hydrogen Absorption. *Appl. Phys. A: Mater. Sci. Process.* **1983**, *32*, 169–182.
- (41) De Marco, M. O.; Li, Y.; Li, H.-W.; Edalati, P.; Floriano, R. Mechanical Synthesis and Hydrogen Storage Characterization of MgVCr and MgVTiCrFe High-Entropy Alloy. *Adv. Eng. Mater.* **2020**, *22*, No. 1901079.
- (42) Liu, J.; Xu, J.; Sleiman, S.; Ravalison, F.; Zhu, W.; Liu, H.; Cheng, H.; Huot, J. Hydrogen Storage Properties of V_{0.3}Ti_{0.3}Cr_{0.2}Mn_{0.1}Nb_{0.05} High-Entropy Alloy. *Int. J. Hydrogen Energy* **2022**, *47*, 25724–25732.
- (43) Liu, J.; Xu, S.; Sleiman, X.; Chen, S.; Zhu, H.; Cheng, H.; Huot, J. Microstructure and Hydrogen Storage Properties of Ti-V-Cr Based BCC-Type High-Entropy Alloys. *Int. J. Hydrogen Energy* **2021**, *46*, 28709–28718.
- (44) Zhao, H.; Yao, P.; Zhao, Y.; Zeng, Z.; Xia, C.; Yang, T. Microstructure and Hydrogen Storage Properties of Zr-Based AB₂-Type High-Entropy Alloys. *J. Alloys Compd.* **2023**, *960*, No. 170665.
- (45) Chen, H.-L.; Mao, H.; Chen, Q. Database Development and CALPHAD Calculations for High-Entropy Alloys: Challenges, Strategies, and Tips. *Mater. Chem. Phys.* **2018**, *210*, 279–286.
- (46) Zepon, G.; Leiva, D. R.; Strozi, R. B.; Bedoch, A.; Figueroa, S. J. A.; Ishikawa, T. T.; Botta, W. J. Hydrogen-Induced Phase Transition of MgZrTiFe0.5Co0.5Ni0.5 High-Entropy Alloy. *Int. J. Hydrogen Energy* **2018**, *43* (4), 1702–1708.
- (47) Chen, J.; Huang, H.; Xu, T.; Lv, Y.; Liu, B.; Zhang, B.; Yuan, J.; Wu, Y. Enhancement of Vanadium Addition on Hydrogen Storage Properties of High-Entropy Alloys TiZrFeMnCrVx. *Int. J. Hydrogen Energy* **2024**, *50*, 1223–1233.
- (48) Martinez-Garcia, A.; Estrada-Guel, I.; Reguera, E.; Amaro-Hernandez, R.; González, S.; Garay-Reyes, C. G.; Martínez-Sánchez, R. Design and Mechanosynthesis of Low-Weight High-Entropy Alloys with Hydrogen Storage Potential Properties. *Int. J. Hydrogen Energy* **2024**, *50*, 670–684.
- (49) Wang, Z.; Huang, Y.; Yang, Y.; Wang, J.; Liu, C. T. Atomic-Size Effect and Solid Solubility of Multicomponent Alloys. *Scr. Mater.* **2015**, *94*, 28–31.
- (50) Poletti, M. G.; Battezzati, L. Electronic and Thermodynamic Criteria for the Occurrence of High-Entropy Alloys in Metallic Systems. *Acta Mater.* **2014**, *75*, 297–306.
- (51) Toda-Caraballo, I.; Rivera-Díaz-del-Castillo, P. E. J. A Criterion for the Formation of High-Entropy Alloys Based on Lattice Distortion. *Intermetallics* **2016**, *71*, 76–87.
- (52) King, D. J. M.; Middleburgh, S. C.; McGregor, A. G.; Cortie, M. B. Predicting the Formation and Stability of Single-Phase High-Entropy Alloys. *Acta Mater.* **2016**, *104*, 172–179.

- (53) Luo, L.; Chen, L.; Li, L.; Liu, S.; Li, Y.; Li, C.; Li, L.; Cui, J.; Li, Y. High-Entropy Alloys for Solid Hydrogen Storage: A Review. *Int. J. Hydrogen Energy* **2024**, *50*, 406–430.
- (54) Ma, J.; Huang, C. High-Entropy Energy Storage Materials: Synthesis and Application. *J. Energy Storage* **2023**, *66*, No. 107419.
- (55) Zepon, G.; Silva, B. H.; Zlotea, C.; Botta, W. J.; Champion, Y. Thermodynamic Modelling of Hydrogen-Multicomponent Alloy Systems: Calculating Pressure-Composition-Temperature Diagrams. *Acta Mater.* **2021**, *215*, No. 117070.
- (56) Ponsoni, J. B.; Aranda, V.; Nascimento, T. S.; Strozi, R. B.; Botta, W. J.; Zepon, G. Design of Multicomponent Alloys with C14 Laves Phase Structure for Hydrogen Storage Assisted by Computational Thermodynamics. *Acta Mater.* **2022**, *240*, No. 118317.
- (57) Mohammadi, A.; Ikeda, Y.; Edalati, P.; Mito, M.; Grabowski, B.; Li, H.-W.; Edalati, K. High-Entropy Hydrides for Fast and Reversible Hydrogen Storage at Room Temperature: Binding-Energy Engineering via First-Principles Calculations and Experiments. *Acta Mater.* **2022**, *236*, No. 118117.
- (58) Edalati, P.; Floriano, R.; Edalati, K.; Mohammadi, A.; Li, Y.; Zepon, G.; Li, H.-W. Reversible Room Temperature Hydrogen Storage in High-Entropy Alloy TiZrCrMnFeNi. *Scr. Mater.* **2020**, *178*, 387–390.
- (59) Andrade, G.; Silva, B. H.; Zepon, G.; Floriano, R. Hydrogen Storage Properties of Zr-Based Multicomponent Alloys with C14-Laves Phase Structure Derived from the Zr–Cr–Mn–Fe–Ni System. *Int. J. Hydrogen Energy* **2024**, *51*, 246–254.
- (60) Andrade, G.; Zepon, G.; Edalati, K.; Mohammadi, A.; Ma, Z.; Li, H.-W.; Floriano, R. Crystal Structure and Hydrogen Storage Properties of AB-Type TiZrNbCrFeNi High-Entropy Alloy. *Int. J. Hydrogen Energy* **2023**, *48*, 13555–13565.
- (61) Floriano, R.; Zepon, G.; Edalati, K.; Fontana, G. L. B.; Mohammadi, A.; Ma, Z.; Li, H.-W.; Contieri, R. J. Hydrogen Storage Properties of New A3B2-Type TiZrNbCrFe High-Entropy Alloy. *Int. J. Hydrogen Energy* **2021**, *46*, 23757–23766.
- (62) Floriano, R.; Zepon, G.; Edalati, K.; Fontana, G. L. B.; Mohammadi, A.; Ma, Z.; Li, H.-W.; Contieri, R. J. Hydrogen Storage in TiZrNbFeNi High-Entropy Alloys, Designed by Thermodynamic Calculations. *Int. J. Hydrogen Energy* **2020**, *45*, 33759–33770.
- (63) Toby, B. H. R Factors in Rietveld Analysis: How Good Is Good Enough? *Powder Diffr.* **2006**, *21*, 67–70.
- (64) Zhu, Y.; Yang, X.-S.; Xu, Z.-L.; Tsui, C.-P.; Zhou, Q.; Tang, R.; Xiao, F.; Chan, K. Development of AB2-Type TiZrCrMnFeCoV Intermetallic High-Entropy Alloy for Reversible Room-Temperature Hydrogen Storage. *J. Energy Storage* **2024**, *75*, No. 109553.
- (65) Liang, J.; Li, G.; Ding, X.; Li, Y.; Wen, Z.; Zhang, T.; Qu, Y. Effect of C14 Laves/BCC on Microstructure and Hydrogen Storage Properties of (Ti_{32.5}V_{27.5}Zr_{7.5}Nb_{32.5})_{1-x}Fe_x (x = 0.03, 0.06, 0.09) High-Entropy Hydrogen Storage Alloys. *J. Energy Storage* **2023**, *73*, No. 108852.
- (66) Zhao, H.; Yao, P.; Zhao, Y.; Zeng, Z.; Xia, C.; Yang, T. Microstructure and Hydrogen Storage Properties of Zr-Based AB2-Type High-Entropy Alloys. *J. Alloys Compd.* **2023**, *960*, No. 170665.
- (67) Komeili, M.; Arabi, H.; Pourarian, F. Structural Investigation and Hydrogenation Properties of TiZrXMnFeNi (X = Cr, Mo, and W) High-Entropy Alloys. *J. Alloys Compd.* **2023**, *967*, No. 171672.
- (68) Garcés, J. The Configurational Entropy of Mixing of Interstitial Solid Solutions. *Appl. Phys. Lett.* **2010**, *96*, No. 161904.
- (69) Ohta, T. *Energy Carriers and Conversion Systems with Emphasis on Hydrogen; Life Support Systems (EOLSS)*, 2009; Vol. 2.
- (70) Takeuchi, A.; Inoue, A. Mixing Enthalpy of Liquid Phase Calculated by Miedema's Scheme and Approximated with Sub-Regular Solution Model for Assessing the Forming Ability of Amorphous and Glassy Alloys. *Intermetallics* **2010**, *18*, 1779–1789.
- (71) Dangwal, S.; Edalati, K. High-Entropy Alloy TiV₂ZrCrMnFeNi for Hydrogen Storage at Room Temperature with Full Reversibility and Good Activation. *Scr. Mater.* **2024**, *238*, No. 115774.
- (72) Dangwal, S.; Edalati, K. Significance of Interphase Boundaries on Activation of High-Entropy Alloys for Room-Temperature Hydrogen Storage. *Int. J. Hydrogen Energy* **2024**, *50*, 626–636.
- (73) Aranda, V.; Leiva, D. R.; Huot, J.; Botta, W. J.; Zepon, G. Hydrogen Storage Properties of the TiVFeZr Multicomponent Alloy with C14-Type Laves Phase Structure. *Intermetallics* **2023**, *162*, No. 108020.
- (74) He, Y.; Su, Y.; Yu, H.; Chen, C. First-Principles Study of Hydrogen Trapping and Diffusion at Grain Boundaries in γ-Fe. *Int. J. Hydrogen Energy* **2021**, *46*, 7589–7601.
- (75) Ma, Z. X.; Xiong, X. L.; Zhang, L. N.; Zhang, Z. H.; Yan, Y.; Su, Y. J. Experimental Study on the Diffusion of Hydrogen Along Individual Grain Boundaries in Nickel. *Electrochim. Commun.* **2018**, *92*, 24–28.
- (76) Fontana, G. L. B. G.; Edalati, P.; Dangwal, S.; Edalati, K.; Strozi, R. B.; Floriano, R. Crystal Structure and Hydrogen Storage Properties of ZrNbFeCo Medium-Entropy Alloy. *Intermetallics* **2025**, *176*, No. 108576.
- (77) Zhou, P.; Zhang, J.; Bi, J.; Xiao, X.; Cao, Z.; Zhan, L.; Shen, H.; Lu, M.; Li, Z.; Zhao, Y.; Wang, L.; Yan, M.; Chen, L. Underlying Factors of Mega Pressure Hysteresis in Cerium-Rich CaCu₅-Type Metal Hydrides and Effective Modification Strategies. *J. Mater. Chem. A* **2023**, *11*, 25963–25972.
- (78) Zhou, P.; Xiao, X.; Zhu, X.; Chen, Y.; Lu, W.; Piao, M.; Cao, Z.; Lu, M.; Fang, F.; Li, Z.; Jiang, L.; Chen, L. Machine Learning Enabled Customization of Performance-Oriented Hydrogen Storage Materials for Fuel Cell Systems. *Energy Storage Mater.* **2023**, *63*, No. 102964.
- (79) Dangwal, S.; Ikeda, Y.; Grabowski, B.; Edalati, K. Machine Learning to Design High-Entropy Alloys with Desired Enthalpy for Room-Temperature Hydrogen Storage: Comparison with Density Functional Theory and Experiments. *Chem. Eng. J.* **2024**, *493*, No. 152606.



CAS BIOFINDER DISCOVERY PLATFORM™

BRIDGE BIOLOGY AND CHEMISTRY FOR FASTER ANSWERS

Analyze target relationships,
compound effects, and disease
pathways

Explore the platform

